Projection Microstereolithography Using Digital Micro-mirror Dynamic Mask

C. Sun, N. Fang, D. M. Wu, and X. Zhang[a)]

Department of Mechanical and Aerospace Engineering, University of California Los Angeles, Los Angeles, CA 90095

ABSTRACT

We present in this paper the development of a high-resolution projection micro-stereolithography (PμSL) process by using the Digital Micromirror Device (DMD™, Texas Instruments) as a dynamic mask. This unique technology provides a parallel fabrication of complex 3D microstructures used for micro electro-mechanical systems (MEMS). Based on the understanding of underlying mechanisms, a process model has been developed with all critical parameters obtained from the experimental measurement. By coupling the experimental measurement and the process model, the photon-induced curing behavior of the resin has been quantitatively studied. The role of UV doping has been thereafter justified, as it can effectively reduce the curing depth without compromising the chemical property of the resin. The fabrication of complex 3D microstructures, such as matrix, and micro-spring array, with the smallest feature of 0.6 μm, has been demonstrated.

Keywords: 3D microfabrication; projection microstereolithography; dynamic mask; polymer

[a)] Electronic mail: xiang@microlab.seas.ucla.edu

I. INTRODUCTION

In the past 20 years, continuous investment has led to the rapid advancement of micro electro-mechanical systems (MEMS) technology. MEMS technology, known as chip-level integration of mechanical sensors and actuators, provides attractive advantages of low cost manufacturing, high sensitivity, low power consumption, and high function integration. Beyond laying down planar electronic circuits on the semiconductor substrate, MEMS technologies extend the micro-fabrication into the vertical dimension as required in manufacturing micro-mechanical devices for ultimate performance. However, in the past twenty years, MEMS technology has heavily relied on the IC-micromachining as the primary established technology for micro-fabrication.

Typically, IC-micromachining technology, which includes both surface and bulk micromachining technology, is used in fabricating MEMS devices. Due to the nature of the silicon process, IC-micromachining technology is rather limited in its ability to fabricate complex microstructures, producing only simple geometric shapes from isotropic and anisotropic etching. In addition, IC-micromachining technology can only be applied to materials such as common semiconductors, metals, and dielectric materials [1].

MEMS technology is now demanding that micro-fabrication technology be capable of fabricating complex microstructures from diverse materials, such as ceramic, metal alloy, polymer, and semiconductor materials. MEMS technology will advance tremendously if more complex microstructures can be fabricated.

The LIGA process (German acronym that stands for lithography, electroplating, and molding) builds high-aspect ratio microstructures by incorporating thick resist layers under masked x-ray or laser irradiation [2]. However, the LIGA process is limited in fabricating $2\frac{1}{2}$-dimensional microstructures while fabrication of truly three-dimensional(3D) microstructure remains a challenge. Several free-forming techniques have been explored in solving the critical issue of 3D micro-fabrication. Three-dimensional laser chemical vapor deposition (3D-LCVD) technology fabricates the microstructures by laser-induced chemical vapor deposition (LCVD). The shape of the micro parts is defined by the scanning of a focused laser spot [3]. Electrochemical fabrication (EFAB) technology has been developed as an extension to the LIGA process in order to fabricate complex 3D metal microstructures [4]. The electro-chemically deposited metal layers are defined as electrode masks and a planarizing procedure controls the layer thickness. Nevertheless, the 3D-LCVD and EFAB are still suffering from the drawbacks due to the limited materials that can be incorporated with this process.

As a novel micro-fabrication process, micro-stereolithography (μSL) has been developed to produce high precision, 3D MEMS devices [5,6]. In principle, μSL utilizes focused light spot scanning over the photo curable resin surface and then a light-induced photo-polymerization occurs, constructing solid microstructures. With focused light spot scanning, a tightly focused laser spot permits little micron spatial resolution. Furthermore, sub-micron resolution has been achieved through a two-photon polymerization process [7]. Not limited to polymeric microstructure, fabrication of ceramic and metal green bodies with complex geometry shapes has

also been demonstrated by μSL. This was accomplished by mixing UV curable resin with fine powders [6,8].

Although the fabrication of individual devices can be accomplished in a few hours, the serial nature of the direct writing process limits the yield rate for mass production. To overcome the limitation, a parallel process has been proposed whereby each layer is fabricated simultaneously while the mask pattern is projected onto the liquid resin surface [9]. Being fully compatible with the silicon process, this process permits the integrated fabrication of the micro device onto the IC chip. However, this process has a major drawback: it requires a great number of masks, which significantly increases the processing time and cost. To avoid the difficulties involved in the multiple mask process, this process has been revised by replacing the multiple mask sets with the dynamic mask. The dynamic mask is capable of modulating the multiple mask-pattern electronically, without physically replacing the mask for each layer. The commercially available and large format dynamic mask, is the micro display device, which was initially developed for the high-resolution projection display.

Along with the endless effort to develop large area and high-resolution display techniques, recent progress of the high-resolution SLM devices has generated the commercialization of compact SLM chips, which contain as much as 1280 x 1024 pixel elements, with a typical pixel size of 17 μm to 30 μm. These commercial SLM products readily provide a convenient dynamic pattern generator to replace the photo masks in Takagi's design [9]. In fact, the idea of using a μSL projection process with a liquid crystal display (LCD) mask was first demonstrated by Bertsch *et al.* [10]. As the process time, in projection μSL, was

reduced dramatically, microstructures containing more than 1000 layers could now be fabricated within a few hours.

However, the LCD technique has some intrinsic drawbacks that hamper its performance. Not only do the large pixel sizes and low filling ratio prevent the device from being more compact, but also the low switching speed (~20ms) and low optical density of the refractive elements during the ***OFF*** mode hinder the contrast of the transmitted pattern. What's more, in general, LCD's UV light absorption is significantly higher during the ***ON*** mode. Therefore, the μSL process in Bertch's system cannot take advantage of a variety of commercial UV curable resins that are optimized for stereolithography [11].

All the above-mentioned difficulties limit further improvement of the micro-stereolithography system with the dynamic mask using LCD technology. Meanwhile, a competing technology in the field of digital display is the Digital Micromirror Device (DMD) [12]. This novel reflective type SLM device, invented by Texas Instruments, is drawing increased attention due to its excellent performance.

Using the DMD chip as a dynamic mask generator, we present in this paper the development of the high-resolution projection micro-stereolithography (PμSL) system. For the first time, the process model of the projection micro-stereolithography system has been studied while the characterization experiment has been carried out to analyze the critical parameters. The UV doping technique has been investigated to further enhance the process resolution.

II. PROJECTION MICROSTEREOLITHOGRAPHY SYSTEM

A. Principle

The high-resolution PμSL apparatus has been developed by using the DMD as the dynamic mask. Similar to the conventional stereolithography process, the PμSL fabricates the complex 3D microstructures in a layer-by-layer fashion [14]. The shapes of these constructed layers are determined by slicing the design CAD model with a series of closely spaced horizontal planes. By taking the sliced layer patterns in the electronic format, the mask patterns are dynamically generated as bitmap images on a computer-programmable array of digital micro-mirrors on the DMD chip. The light illuminated on the DMD chip is shaped according to the defined mask pattern, and then, the modulated light is transferred through a reduction lens. Hence, an image is formed on curable resin surface with a reduced feature size.

In each layer, the illuminated area is solidified simultaneously under one exposure, while the dark regions remain liquid. After the fabrication of one layer, the substrate is immersed into the UV curable resin and the new layer is fabricated on top of the existing structure. A complex, geometrically shaped microstructure can be fabricated by building all the layers sequentially and stacking them from bottom to top.

B. System overview

The developed PμSL system is schematically shown in Figure 1. It is an integration of many sub-systems, all of which function in cooperation to provide correct exposure and layer thickness control. The five major components are identified as: the Digital Micromirror device

((DMD, as the dynamic mask), a projection lens, a UV light source, a motorized translation stage, and a vat containing UV curable resin.

The dynamic mask is the core component of the PμSL system that determines the shape of the fabricated microstructure. As the dynamic mask, the DMD modulates the light by collectively controlling the micro-mirror arrays to switch the light on and off on each individual pixel. The arrays of aluminum micro-mirrors are anchored on top of addressable SRAM CMOS circuitries, and two positions are permitted for the mirror to tilt at +10 or –10 degrees along its diagonal. By toggling the voltage applied to the individual micro-mirror, the mirror can be switched between stable positions with the light reflecting “on” and “off” directions.

The DMD promotes many unique advantages over the conventional LCD spatial light modulator. The DMD has smaller pixel size as well as narrow gaps between pixels, which allow higher display resolution and better intensity uniformity. Moreover, ultra-flat aluminum micro-mirrors enable high modulation efficiency of UV illumination. The efforts in enhancing the process resolution will benefit tremendously by using UV light as the shorter wavelength light source because the shorter wavelength leads to higher spatial solution as determined in diffractive optics. On the other hand, shorter wavelength corresponds to higher photon energy that helps to enforce the mechanical strength of polymerized microstructures. Furthermore, the fast switching speed in DMD enables more precise control of the exposure time, which is particularly important in achieving grayscale intensity modulation at pixel level. Thus, as concluded in Table 1, the major advantages of DMD enable the development of the high-resolution projection micro-stereolithography system.

Since the uniformity of the light illumination is the critical factor that determines the process reliability, it is necessary to introduce the *fly-eye* type optical homogenizer at the mercury lamp output. This component provides uniform illumination on the DMD chip by maintaining the intensity fluctuation within ± 5%. The 5:1 projection lens is then chromatically corrected at a wavelength of 364 nm with the spatial resolution of 1.1 μm. Thus, Mercury I-line emission is selected as the illumination light source. Layer thickness is controlled by the computerized mechanical translation stage with a translation precision of 0.1 μm. The whole process is coordinated with the PC-based control unit.

The UV curable resin is the mixture of the monomer and photo-initiator. Under the UV light illumination, the photo-initiator absorbs the incident photons and generates radicals. The radicals react with the monomer molecules to form larger reactive molecules. These larger reactive molecules, in turn, have the ability to react with other monomers and form longer reactive molecules. The reactive molecules will keep growing until two of them meet together and form a stable polymer chain. The solidified polymer structure will eventually be constructed by the cross-linking of those polymer chains.

In our process, the UV curable resin consists of 1,6-hexanedioldiacrylate (HDDA, $[H_2C{=}CHCO_2(CH_2)_3\text{-}]_2$) as the low viscosity monomer and Benzoin ethyl ether (BEE, $C_6H_5CH(OC_2H_5)COC_6H_5$) as the photo-initiator. According to our previous study, an important amount of UV absorber has been mixed with the UV curable resin to adjust the curing depth.

III. THREE-DIMENSIONAL MICRO-FABRICATION

Fabrications of several complex 3D microstructures have been demonstrated (Figure 2). The micro-matrix is fabricated by 110 layers with the layer thickness of 5 μm [Figure 2(a)]. The matrix is made up of three freestanding mesh layers suspended on an array of vertical posts, separated at identical distances in a vertical direction. The non-uniform line width of suspended wires presents the *cross-talk* effect, which is induced by light diffraction. On-going experiments are being aimed to investigate the *cross-talk effect*, its mechanisms, and ways to reduce it.

By adding more sliced layers, a microstructure with even higher aspect ratio can also be built. The micro rod array, (Figure 2(b)), consists of an array of rods with an extremely high aspect ratio. The rods shown in Figure 2(b) present uniform dimensions with 30 μm in diameter, and 1000 μm in height, which correspond to the aspect ratio of 33:1.

The PμSL is not only advanced in constructing high aspect ratio structures, but it also enables the fabrication of sophisticated 3D microstructures, which is difficult to achieve by conventional micro fabrication processes. The PμSL accomplishes this by fabricating an array of 3 x 3 micro-coil into 108 layers, with each layer having a thickness of 5 μm. The diameter of the coil is 150 μm and the wire diameter is 15 μm [Figure 2(c)]. The ultimate feature size control is demonstrated through the fabrication of suspended beams with a diameter of 0.6 μm [Figure 2(d)].

IV. PROCESS CHARACTERIZATION

Spatial resolution is a critical issue to the PμSL process. Two fundamental factors limiting the spatial resolution of PμSL systems are optical resolution of projected image, and the

physical-chemical characteristics of chemical resin. Based on diffractive optics, a numerical model is developed to reveal the fundamental mechanism underlying the physical process. This numerical model is also associated with the experimental measurement which determines the process parameters.

A. Process model

The coordinate system adopted in the process model is shown in Figure 3. The ***XY*** plane coincides with the surface of the UV curable resin as well as the focused image plane. The ***Z*** axis is normal to the resin surface, with the positive ***Z*** directed downward into the resin.

Due to the diffractive nature of light, instead of focusing on a single point, a light spot emitted from an object will rather smear out into a blurred spot at the image plane. The spread of radiation flux is described by the *point-spread function* (PSF) [15]. Because of the incoherency of the light reflected from DMD, the flux-density contribution of its elements are additive. An image is formed by the linear superposition of flux-density contributions of the light spot that emitted from the object.

In this work, Guassian distribution is used as the first order approximation of PSF to describe the flux-density contribution of light spot from the image plane [16]. Therefore, the flux density contribution $\boldsymbol{E}(\boldsymbol{x})$ at certain position $\boldsymbol{x}$ is defined as:

$$E(x) = E_0 \exp\left(-x^2 / w_0^2\right) \qquad (1)$$

where E_0 is the peak intensity, and w_0 is the Guassian radius. The Guassian radius provides a quantitative measure of the spreading width of the spot light source, and therefore, determines the range of the *cross-talk* between imaged light spots.

As illustrated in Figure 3, a square pattern with the dimension of $2w_x$ and $2w_y$, is focused onto the surface of UV curable resin. The intensity distribution of the image along the ***xz***-plane is characterized in Figure 4 as the solid line. The dash lines represent the intensity distribution corresponding to a single-spot light source. The E_{MAX} is the peak value intensity distribution, whereas the E_0 is the peak intensity of the Guassian distribution of each individual spot light source. The designed pattern width, $2w_x$, is shown as the dot-dash line.

Numerically, the intensity distribution at the image plan is obtained from the summation of the Guassian distribution of each individual spot light source from the object. Assume a line pattern has finite width along the ***X*** axis and infinite length along the ***Y*** axis as projected onto the resin surface. The cross-section of intensity profile along the ***X*** axis can be calculated (Figure 5). Considering the working wavelength and numerical aperture (NA) of the projection lens, we assume that the Guassian radius of the PSF is w_0 =5μm. The line width is varied from 1 pixel to 5 pixels, which corresponds to the image width of 3.4 μm to 17 μm, respectively.

Figure 5 shows the evolution of the intensity profile with increasing line width. The intensity distribution presents a bullet-like shape at the line width closer to the Guassian radius, while the peak intensity E_{MAX} can be obtained by increasing the line width. The peak power presents the "flat-top" shape of the intensity profile when the line width is much larger than the Guassian radius. Ideally, the intensity will eventually be saturated when the line width goes to infinity, which is defined as E_{inf}.

The ratio E_{MAX}/E_{inf} depends on the ratio of the pattern dimension w_L and the Guassian radius w_0. The relationship between E_{MAX}/E_0 and w_L/w_0 can be expressed as:

$$E_{MAX} / E_{\inf} = erf\left(\sqrt{2}\frac{w_L}{w_0}\right) \tag{2}$$

where ***erf(x)*** is the error function defined as:

$$erf(x) = \frac{2}{\sqrt{\pi}}\int_0^x \exp(-t^2)dt\ . \tag{3}$$

The general expression of the intensity distribution at the image plane can be described as:

$$\begin{aligned} E(x,y,0) = E_{\inf}\Big\{ & erf\left[\sqrt{2}\left(w_x/2+x\right)/w_0\right] + erf\left[\sqrt{2}\left(w_x/2-x\right)/w_0\right]\Big\} \\ & \cdot\Big\{erf\left[\sqrt{2}\left(w_y/2+y\right)/w_0\right] + erf\left[\sqrt{2}\left(w_y/2-y\right)/w_0\right]\Big\} \end{aligned} \tag{4}$$

Normally, the experimental value of E_m is obtained by measuring the overall intensity of the projected big square pattern using a dimension much greater than the typical Guassian radius. As we noticed in Figure 6, the E_{MAX} is quickly converged to the E_{inf} at w_L/w_0 greater than 2, while the relative error between E_{MAX} and E_{inf} is well below 10^{-5}. Therefore, it is reasonable to assume that E_{inf} can be represented by using the experimental measured E_m. To simplify the preceding discussion, we define the intensity correction term k to represent the ratio E_{MAX} and E_m:

$$k = E_{MAX} / E_m = erf\left(\sqrt{2}\frac{w_L}{w_0}\right) \tag{5}$$

Assume the light incident affecting the resin moves from the top and then propagates along the positive direction of the ***Z*** axis. Thus, UV light absorption of the resin can be described by the Beer-Lambert Law. The irradiation, ***E(x,y,z)***, at any point within the resin is defined as:

$$E(x, y, z) = E(x, y, 0)\exp(-z / D_p) \tag{6}$$

where $\boldsymbol{D_p}$ is the light penetration depth of the resin, which is defined as the depth within the resin where irradiation drops to 1/e of the intensity on the surface. Hence, the photo-induced polymerization can be characterized as the "working curve equation", which is the analytic model generally accepted in the stereolithography process [13,17].

$$C_d = D_p \ln\left(E_{\max} / E_c\right) = D_p \ln\left(kE_m / E_c\right) = D_p \ln\left(E_{\max} / E_c^*\right) \tag{7}$$

where $E_c^* = E_c / k$ is the **effective critical energy** that can be directly calculated from the experimental measurements. On the other hand, the **effective penetration depth** D_p^* is defined as the depth, where the exposure drops to 1/e of the E_m. However, as we discussed, the intensity on the resin surface is $E_{\max}$ instead of E_m. The measured D_p^* is the depth, where the intensity is attenuated to $E = E_0 / e = E_{\max} / ke$. Therefore, the penetration depth of the resin can be expressed as:

$$D_p = \frac{D_p^*}{1 + \ln k}. \tag{8}$$

B. Experimental analysis

In this experiment, a test pattern consisting of fine thread with different widths is projected onto a special designed test cell (Figure 7). In the test cell, UV curable resin is sandwiched between the top quartz windows and the silicon substrate. To eliminate the influence

of the UV light reflected by the substrate, 500 μm thick spacers are placed on the edge to keep the reaction region away from the substrate. The designed test pattern is shown in Figure 8. The parallel fine threads are separated at 60 pixels to eliminate their influences on each other. The big rectangle blocks are designed to ensure strong adhesion of the polymerized thread onto the quartz window after rinsing. The critical curing parameters, the curing depth, and the curing width, can be obtained by measuring the depth and width of polymerized fine threads under an optical microscope or Scanning Electron Microscope (SEM).

As shown in Figure 9, the experimental measurements of working curves of UV curable resins are obtained by measuring the curing depth under various UV exposures. The curing characterization of UV curable resin with and without UV absorber has been compared. The results indicate that the curing depth is linearly proportional to the natural logarithm of UV exposure, which is in good agreement with the numerical model.

Under the same UV exposure, the resin with 0.3% UV doping has a smaller curing depth. This result coincides with the theoretical expectation that the incident UV light will be greatly attenuated by UV doping and less light can penetrate even deeper to induce the photo-polymerization. Hence, the curing depth is controllable by tuning the concentration of UV doping.

Qualitative results of penetration depth D_p^* and the effective critical exposure E_c^* are obtained by applying the working curve equation (Eq. 7) to analyze the experimental data. The D_p^* is represented by the slope of the working curve, whereas E_c^* is determined by

extrapolating the working curve to intercept with the ***X*** axis. The effective curing depth D_p^* and the effective critical energy E_c^* are the two fundamental parameters that define the photosensitivity of UV curable resin during the process.

By analyzing the working curves, the influences of the pattern line width and UV doping are investigated [Figure 10]. As expected, at different UV doping levels, the E_c^* have similar values within the measurement tolerance while the D_p^* has been significantly reduced by introducing the UV doping. This result indicates that non-reactive UV doping can effectively reduce the penetration depth of the resin with less influence of the chemical reactivity. With the increased line width, the effective critical energy E_c^* decreases from 110 mJ/cm^2 to 74 mJ/cm^2, whereas effective penetration depth D_p^* increases from 34 μm to 39 μm. For resin with 0.3% UV doping and without UV doping, effective penetration depth D_p^* increases from 133 μm to 168 μm.

By fitting Figure 10(b) with Eq. 6, the actual penetration depth D_p of the resin can be obtained. The result shows that the curing depth of the resin is 45 μm with 0.3% UV doping and 163 μm without UV doping. However, while applying the same correction factor ***k*** to study the critical energy, the model cannot fit the experimental data very well. The reason is believed to be the existence of the oxygen in the resin. As we know, oxygen will terminate the radicals in the resin and therefore, inhibit the photo-polymerization reaction. The chemical composition of the resin changes with the presence of the oxygen. Thus, an on-going experiment is being carried out to study the resin's response in an oxygen-free environment.

The measured line width at different UV exposures is shown in Figure 11. The wider polymerized line width is observed at the larger UV exposure. The doped and un-doped resins have similar polymerized line widths under the lower UV exposure. When the exposure is larger than 665 mJ/cm^2, the line width of un-doped resin increases rapidly, while the line width of doped resin increases slowly. This is because the curing width is mainly determined by the amount of UV exposure near the resin surface. When un-doped resin is subject to intense UV exposure, the line width increases rapidly, indicating a strong chemical reaction near the surface region. However, the model developed in this work only considers the line depth rather than line width. The development of more sophisticated numerical models is an ongoing study of the PμSL process.

V. CONCLUSION

In this work, the PμSL system has been successfully developed to fabricate truly 3D microstructures. A process model has been established based on the fundamental study of the underlying physical and chemical mechanisms. The results indicate that the numerical model is in good agreement with the experimental results. The UV curable resin is characterized by the developmental process model with the associated experimental measurements. By introducing 0.3% UV doping, the curing depth of the resin is decreased from 163 μm to 45 μm. The existence of the inhibitor is believed to influence the accuracy of the process model.

ACKNOWLEDGMENT

This work was supported in part Department of Defense Multidicinplinary University Research Initiative (MURI) under Grant No. N00014-01-1-0803, Office of Naval Research (ONR) Young Investigator Award under Grant No. N00014-02-1-0224, and the National Science Foundation (NSF) under Grant No. DMI-0216423.

REFERENCES

[1] S. M. Sze, *Semiconductor Sensors*, (John Wiley & Sons, New York, 1994).

[2] E. W. Becker, W. Ehrfeld, P. Hagmann, A. Maner, D. Munchmeyer, Microelectron. Eng. 4, 35 (1986).

[3] K. Williams, J. Maxwell, K. Larsson, M. Boman, Technical Digest. IEEE International MEMS 99 Conference, 232 (1999).

[4] A. Cohen, G. Zhang, F. Tseng, U. Frodis, F. Mansfeld, P. Will, Technical Digest. IEEE International MEMS 99 Conference, 244 (1999).

[5] Ikuta, K. and Hirowatari, K., Proceedings. IEEE. Micro Electro Mechanical Systems 42 (1993).

[6] X. Zhang, X. N. Jiang, C. Sun, Sensors and Actuators A 77, 149 (1999).

[7] S. Maruo K. Ikuta, Proceedings of 1999 International Symposium on Micromechatronics and Human Science, 173 (1999).

[8] X. N. Jiang, C. Sun, X.Zhang, B. Xu, Y. H. Ye, Sensors and Actuators A 87, 72 (2000).

[9] T. Takagi, N. Nakajima, Proceedings. IEEE. Micro Electro Mechanical Systems 173 (1993).

[10] A. Bertsch, Y. J. Jezequel, C. Andre, J. Photoch. Photobio. A 107**,** 275 (1997).

[11] Huang, S., Heywood, M. I., Young, R. C. D., Farsari, M., Chatwin, C. R., Microprocess. Microsy. 22, 67 (1998).

[12] Larry J. Hornbeck, TI Technical Journal, 15, 7 (1998).

[13] R. E. Meier, TI Technical Journal, 15, 64 (1998).

[14] P. F. Jacobs, *Rapid Prototyping and Manufacturing: Fundamentals of Stereolithography,* (Society of Manufacturing Engineers Publishers, Dearborn, 1992).

[15] E. Hecht, *Optics, 2nd Edition*, (Addison-Wesley, Reading MA, 1988).

[16] G. R. V. Kumar, K. Sayanagi, J. Opt. Soc. Am., 58, 1369 (1968).

[17] Arnost, Reiser. *Photoreactive Polymers - the Science and Technology of Resist,* (John Wiley & Sons, New York, 1989)

Biographies

Cheng Sun received his PhD in Industrial Engineering from Pennsylvania State University in 2002 and MS/BS in Physics from Nanjing University. He is currently the Chief Operating officer at the Center for scalable and Integrated Nanomanufacturing at University of California Los Angeles. His research interest include the novel 3D micro- and nano- fabrication technologies and the device applications.

Nicholas Fang received his PhD in Mechanical Engineering from University of California, Los Angeles in 2004. He is currently an Assistant Research Engineer in the Department of Mechanical Engineering at UCLA. His research interest includes: the 3D micro and nanolithography, design and manufacturing photonic metamaterials and devices, Energy Transfer and Mass Transport Phenomena in Micro/nano/biosystems.

Dongmin Wu received his Master degree in Physics from Nanjing University. He is now a PhD student in the Mechanical and Aerospace Engineering Department at University of California at Los Angeles. His research interest are in 3D micro-fabrication and molecular electronics.

Xiang Zhang graduated with a PhD in Mechanical Engineering from University of California, Berkeley in 1996 and MS/BS in Physics from Nanjing University. He joined Pennsylvania State University in 1996 as an assistant professor. In 2000, He joined University of California at Los Angles and now he is a Professor at Mechanical and Aerospace Engineering Department and Director of NSF Nanoscale Science and Engineering Center (NSEC). *His research interests*

includes: Science and technology in novel micro and nano-scale fabrication and devices, engineering and characterization on nanophotonic and plasmonic materials and structures, sub-wavelength imaging and nanolithography, bio-sensors and nems, transport issues in micro and nano-manufacturing.

LIST OF FIGURES CAPTIONS

Figure 1. Schematic diagram of projection micro-stereolithography (PμSL) apparatus.

Figure 2. 3D complex microstructures fabricated by PμSL process, (a) Micro matrix with suspended beam diameter of 5 μm; (b) High aspect-ratio micro rod array consists of 21 x 11 rods with the overall size of 2mm x 1mm. The rod diameter and height is of 30 μm and 1 mm, respectively; (c) Micro coil array with the coil diameter of 100 μm and the wire diameter of 25 μm; (d) Suspended ultra fine line with the diameter of 0.6 μm.

Figure 3. Schematic diagram of coordinate system adopted for numerical model.

Figure 4. Schematic drawing of the light distribution at the ***xz*** plane (solid). It is formed by superposition of the Guassian distribution (dash). The idea image is with the width of w_x (dot-dash).

Figure 5. Intensity distribution of line with different width at the image plane.

Figure 6. The relationship between E_{MAX}/E_0 and w_L/w_0.

Figure 7. Schematic diagram of PμSL characterization experiment configuration. The UV curable resin is confined within the quartz window and silicon substrate. The thickness of the UV curable resin is controlled by the spacer to eliminate the influence from the substrate.

Figure 8. Pattern of fine thread with different width used for curing depth and curing width measurement experiment.

Figure 9. Measured curing depth vs. incident UV light exposure at different doping levels.

Figure 10 (a) Penetration depth of doped and un-doped resin vs. line width; (b) critical exposure of doped and un-doped resin vs. line width.

Figure 11. Curing width vs. incident UV light exposure at different doping levels.

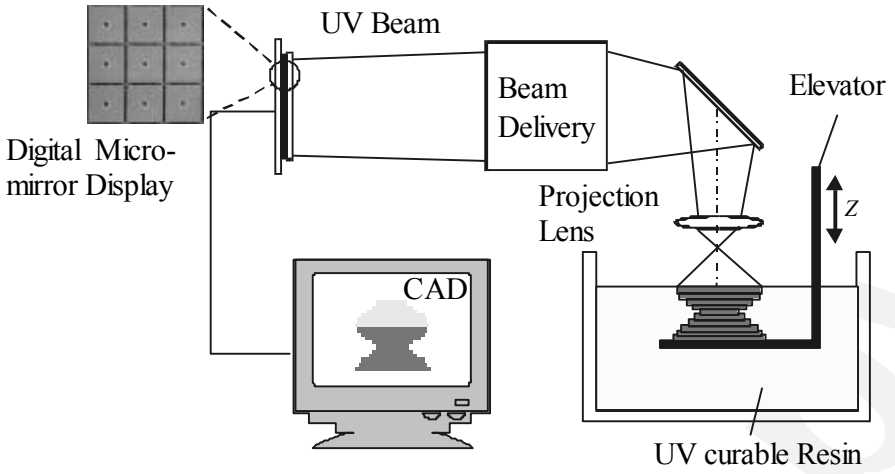

Figure 1. Cheng Sun, et. al., "Projection Microstereolithography Using Digital Micro-mirror Dynamic Mask", *Sensors and Actuators A*

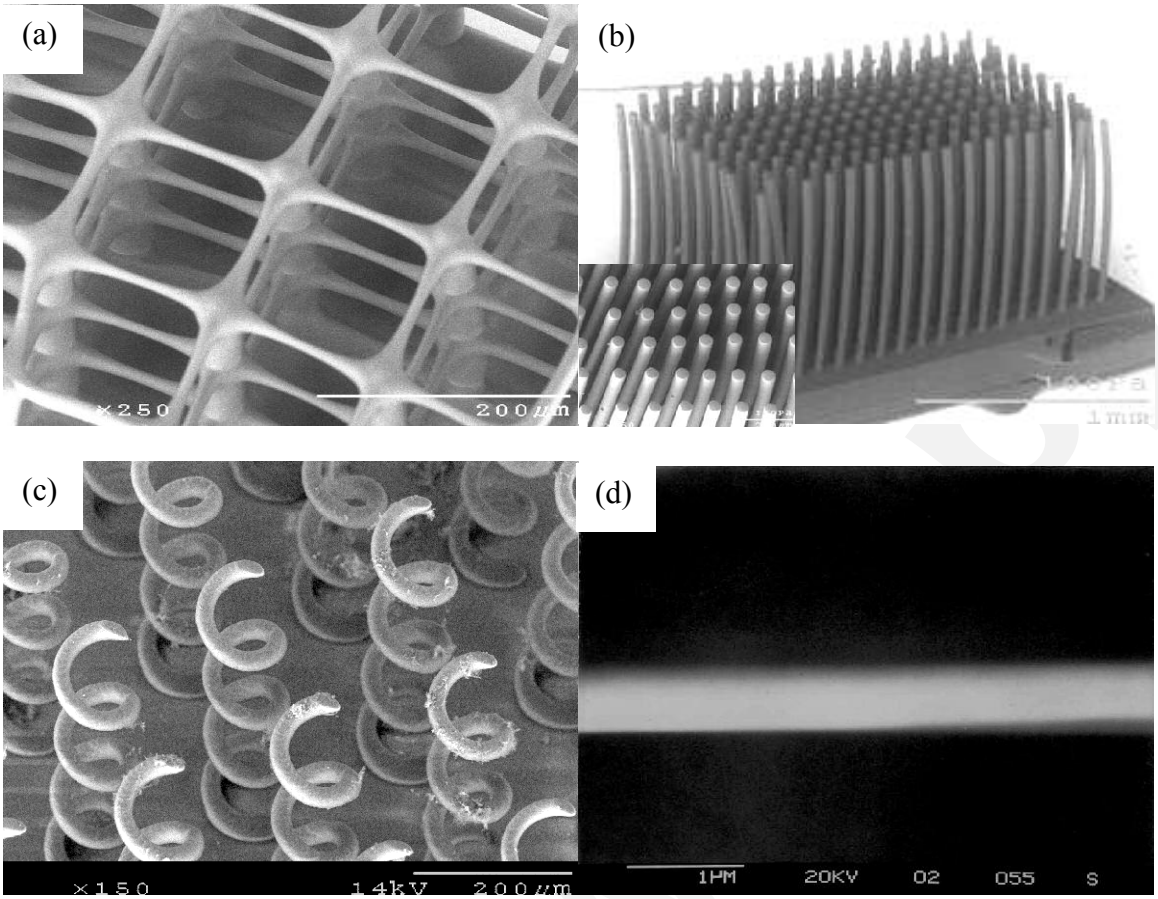

Figure 2. Cheng Sun, et. al., "Projection Microstereolithography Using Digital Micro-mirror Dynamic Mask", *Sensors and Actuators A*

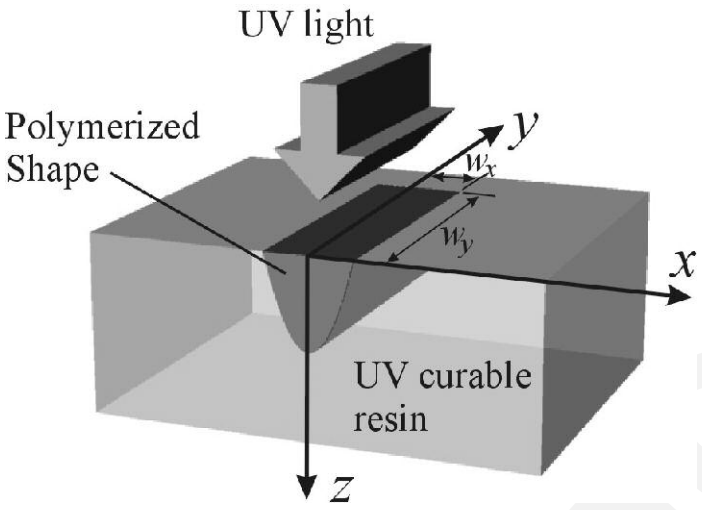

Figure 3. Cheng Sun, et. al., "Projection Microstereolithography Using Digital Micro-mirror Dynamic Mask", *Sensors and Actuators A*

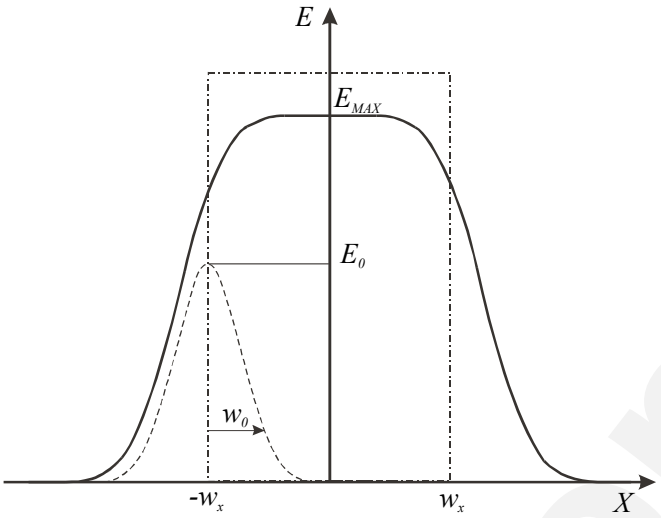

Figure 4. Cheng Sun, et. al., "Projection Microstereolithography Using Digital Micro-mirror Dynamic Mask", *Sensors and Actuators A*

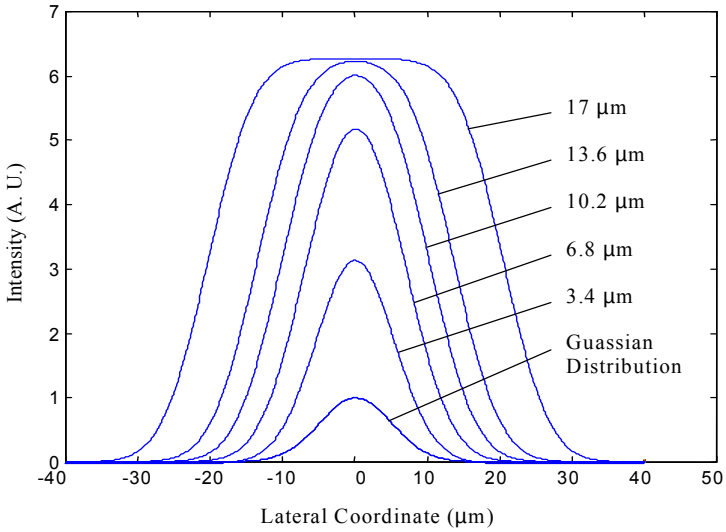

Figure 5. Cheng Sun, et. al., "Projection Microstereolithography Using Digital Micro-mirror Dynamic Mask", *Sensors and Actuators A*

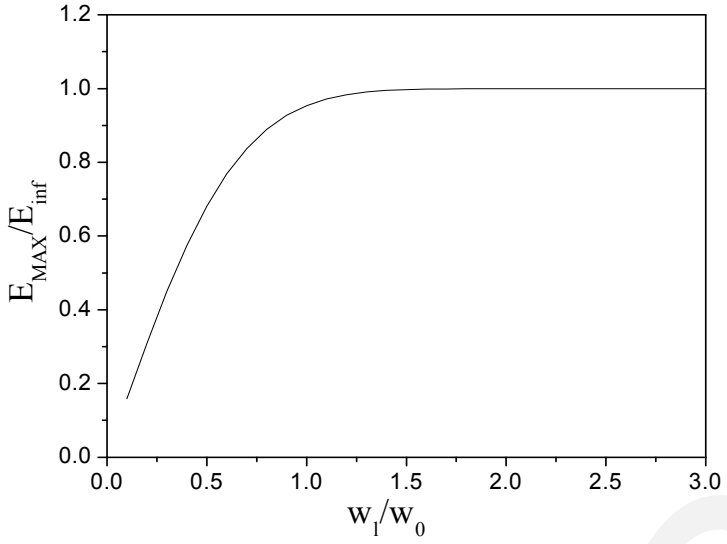

Figure 6. Cheng Sun, et. al., "Projection Microstereolithography Using Digital Micro-mirror Dynamic Mask", *Sensors and Actuators A*

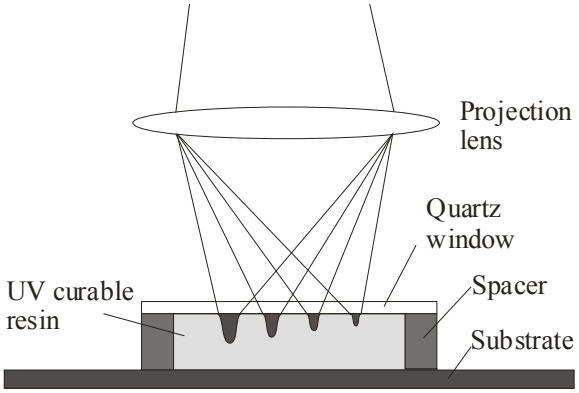

Figure 7. Cheng Sun, et. al., "Projection Microstereolithography Using Digital Micro-mirror Dynamic Mask", *Sensors and Actuators A*

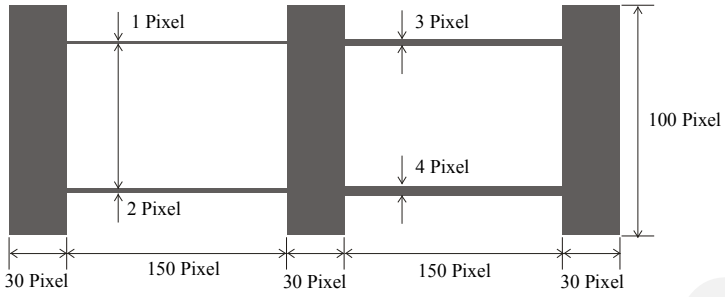

Figure 8. Cheng Sun, et. al., "Projection Microstereolithography Using Digital Micro-mirror Dynamic Mask", *Sensors and Actuators A*

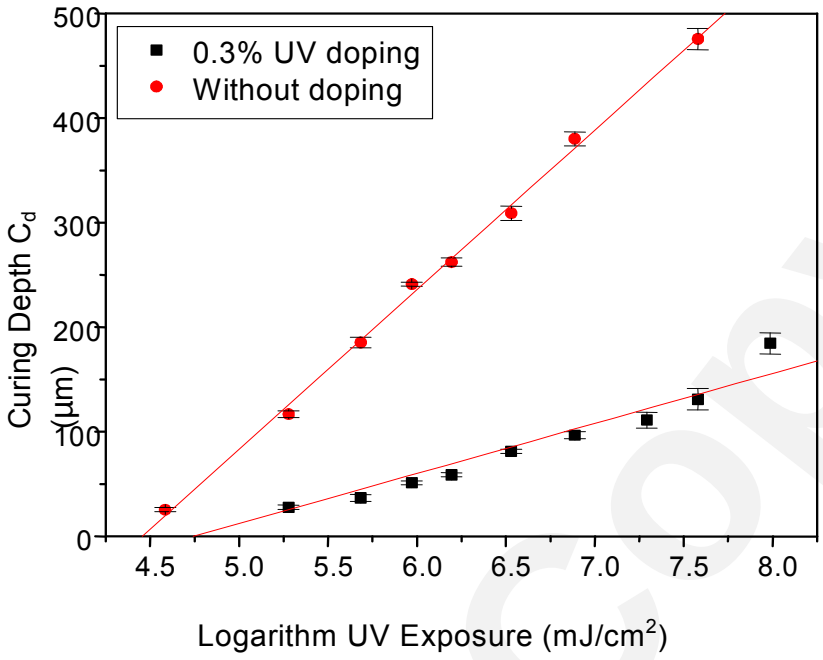

Figure 9. Cheng Sun, et. al., "Projection Microstereolithography Using Digital Micro-mirror Dynamic Mask", *Sensors and Actuators A*

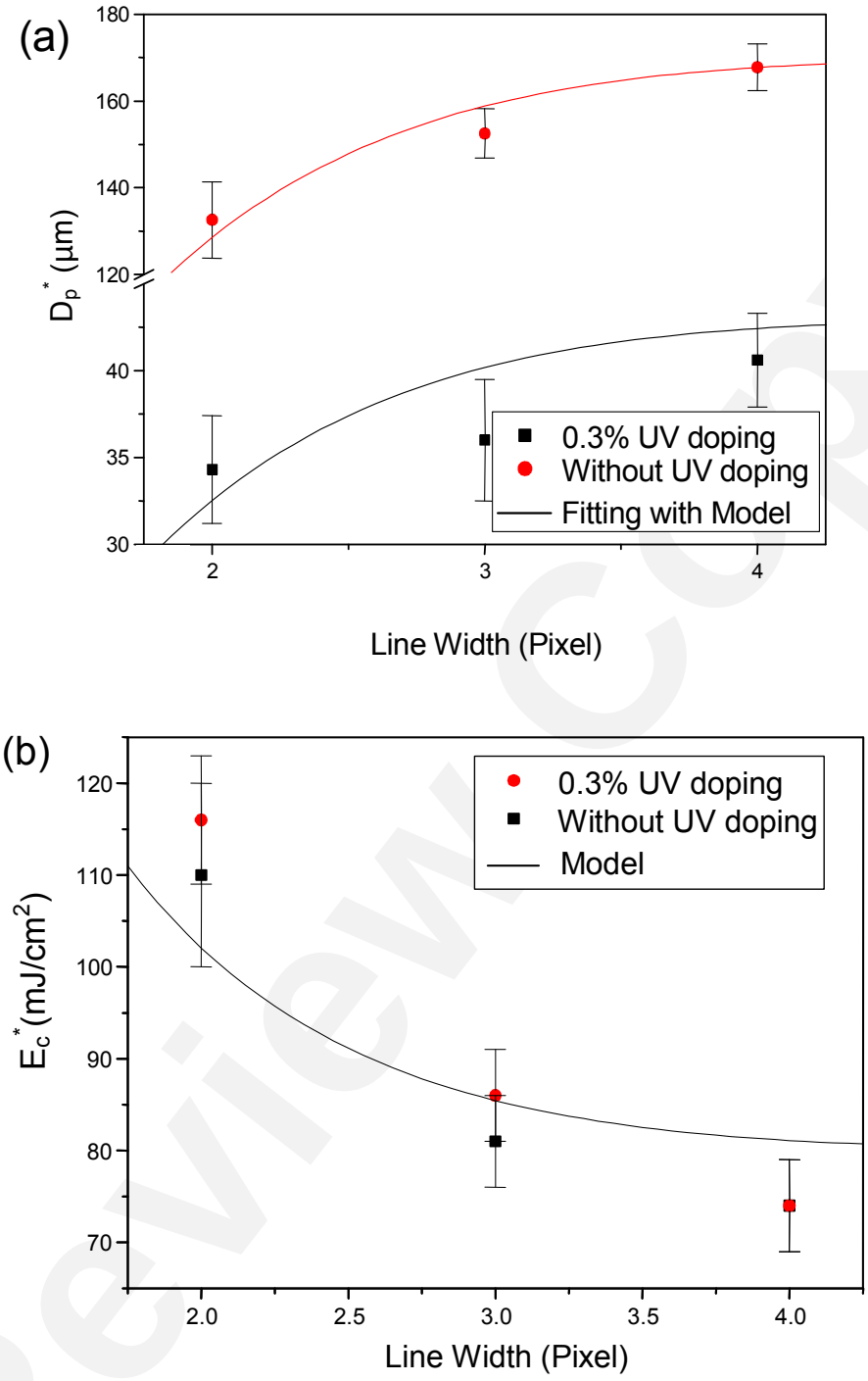

Figure 10. Cheng Sun, et. al., "Projection Microstereolithography Using Digital Micro-mirror Dynamic Mask", *Sensors and Actuators A*

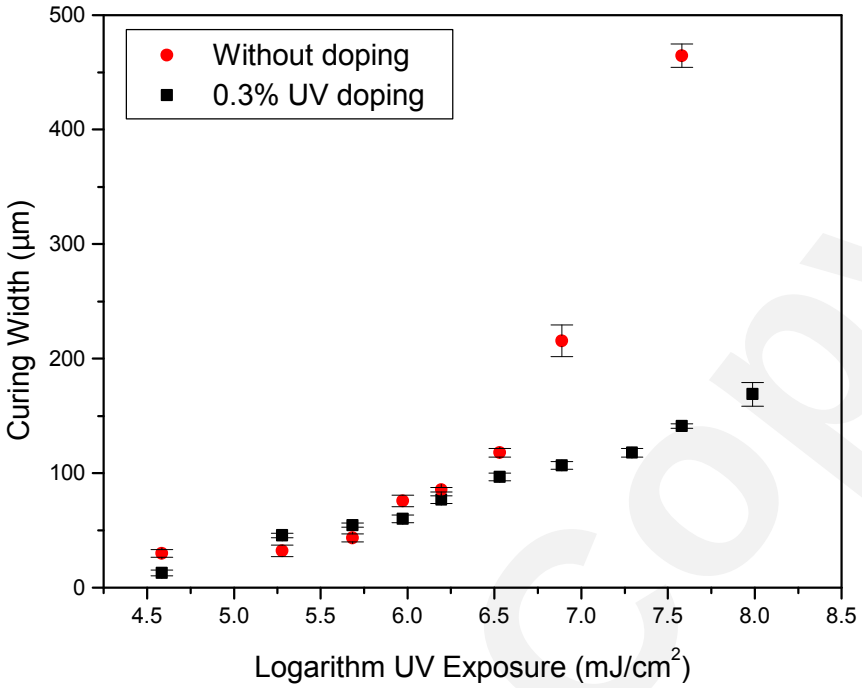

Figure 11. Cheng Sun, et. al., "Projection Microstereolithography Using Digital Micro-mirror Dynamic Mask", *Sensors and Actuators A*

LIST OF TABLES

Table 1. Comparison between DMD and LCD.

	LCD	DMD [13]
UV compatibility	No	Yes
Modulation efficiency	12.5% (Transmission)	88 % (Reflection)
Pitch size	26 μm x 24 μm	14~17 μm
Pixel size	33 μm x 33 μm	13~16.2 μm
Filling ratio	57 %	91%
Contrast	100:1	350:1
Switching speed	20 ms	20 μs